Advanced Materials

ADVANCED MATERIALS
www.advmat.de

RESEARCH ARTICLE

Self-Powered Phototriggered Memristor Array with pW-Level Computing for Monolithic in-Sensor Vision

Xinglong Zhang[1] | Ming Deng[1] | Yiyun Luo[1] | Zijin Zhao[1] | Xiaojun Tan[2] | Xiaosheng Fang[1]

[1]College of Smart Materials and Future Energy, State Key Laboratory of Molecular Engineering of Polymers, Fudan University, Shanghai, P. R. China | [2]Shaoxin Laboratory, Shaoxing, P. R. China

Correspondence: Xiaosheng Fang (xshfang@fudan.edu.cn)

Received: 19 November 2025 | **Revised:** 5 February 2026 | **Accepted:** 13 February 2026

Keywords: 2D Ruddlesden-Popper perovskites | array device | ferroelectric | memristor | photodetector

ABSTRACT

2D Ruddlesden–Popper (RP) hybrid perovskites are widely used in the field of optoelectronic devices due to their high carrier mobility and absorption coefficient. Herein, $BA_2MAPb_2Br_7$ (BMPB) single crystals were synthesized via the quasi-static cooling method, with a thorough investigation of the nucleation mechanism and the intrinsic relationship between rectangular and hexagonal morphologies. Remarkably, BMPB exhibits outstanding memristive performance, featuring an ultrahigh on/off ratio ($\sim 10^5$), ultralow power consumption of ~82.8 pW, and a long retention time (>22 000 s). Leveraging its inherent ferroelectric polarization and optoelectronic properties, we demonstrate a monolithic 5×5 optoelectronic memristor array that unifies sensing, memory, and computing functions. The array device exhibits self-powered performance under 410 nm illumination, with responsivity of 0.96 A/W and detectivity of 2.89×10^8 Jones. Through digital logic circuit design and Vivado verification, we successfully implement solar-tracking time prediction and sunflower growth-stage monitoring. Critically, this integrated architecture enables hardware-level in-sensor computing for real-time applications. Our work provides valuable insights for next-generation in-sensor computing devices, providing a material-level solution based on 2D RP perovskites for energy-efficient AI and IoT systems.

1 | Introduction

Vision is one of the most significant senses for human perception because about 80% of the information that humans obtain comes from the visual system [1–3]. With the advent of the era of artificial intelligence (AI) and the Internet of Things (IoT), there is an urgent need to develop a method that can integrate various sensors and computing units on the same substrate to achieve different levels of processing on a single substrate [4], but this is also very challenging [5]. Therefore, in-sensor computing has become a promising solution, which can significantly improve processing efficiency and simplify hardware systems [6–8]. Recent studies have attempted to construct devices that integrate sensing, storage, and computation based on array imaging sensors. An optoelectronic memristor array device based on ZnO semiconductors was reported [9]. Three visual processing tasks were demonstrated, including image sensing, object tracking, and human motion recognition. Wang et al. reported an in-memory sensing and computing architecture in a ferroelectric-defined 2D photodiode array [10]. The device integrates the function of high-level computing, weight memorization, and high-performance sensing.

However, the current device architecture still relies mainly on vertical integration of different functional layers, making it difficult to achieve sensing, storage, and computing functions on the same material [11–13]. This increases the power consumption of the device and increases the difficulty of its construction

[14]. In the traditional von Neumann architecture, data needs to be frequently transferred between sensors, storage units, and processors. This process consumes much more energy than the actual computation itself, forming a huge power wall and latency bottleneck. The integrated device of sensing, storage, and computing directly performs operations at the location where the sensor obtains data or in adjacent storage units, greatly eliminating or minimizing the need for data movement. This directly saves most of the power consumption caused by data handling, significantly improving the overall energy efficiency of the system [15]. Therefore, there is an urgent need for a highly integrated device similar to the human visual memory system for applications such as AI and IoT.

2D RP hybrid perovskites have shown great prospects to be utilized in light-emitting diodes (LEDs), photodetectors (PDs), and solar cells due to their tunable band gaps, high light absorption factor, and carrier mobility [16–18]. 2D RP perovskites can be depicted as the general formula $(RNH_3)_2A_nX_{3n+1}$, where R is an alkyl or aromatic group, A is a metal cation, and X is a halide anion [19, 20]. Compared to 3D perovskites, 2D RP hybrid perovskites exhibit distinct advantages in optoelectronic performance, primarily attributed to organic cations that enhance exciton binding energy and suppress defect formation [21, 22]. Due to the asymmetry of internal organic small molecules, some 2D RP perovskites exhibit ferroelectric phases at room temperature, and there is a spontaneous polarization electric field within the molecules [23–25]. The introduction of ferroelectric fields can promote the separation efficiency of photo-generated charge carriers, improve the response time of devices, increase photocurrent, and suppress dark current [26]. This feature provides ways of designing photodetectors with high response and low power consumption. Up to now, some literature has reported devices with ferroelectric-optoelectronic multi-field coupling and achieved interesting applications [27–30]. Yang et al. reported a multi-phototransistor and one-memristor array which was based on NbO_x semiconductors [31]. The array could support a variety of optical neural networks when coupled with a classifier network using a one-transistor and one-memristor. Hersam et al. reported a moiré synaptic transistor based on an asymmetric bilayer graphene/hexagonal boron nitride moiré heterostructure, which exhibited robust electronic ratchet states and realized non-volatile injection of charge carriers [32].

At present, a large amount of literature reports on artificial neural network synapses based on non-volatile nano-memristive devices [7, 33, 34]. The integration, power consumption, and read/write speed of random access memory based on memristor are superior to traditional random access memory [35]. The reported types of memristor materials include metal oxides [9, 36, 37] (ZnO, TiO_2) and covalent organic framework [38–40] (COF). There are currently a few reports on memristive devices based on perovskite materials [41], mainly including lead-free perovskites such as CSI [1], CCI [42], CTO [43], and lead-based perovskites like CFMPIB [44, 45], CPC [46]. Herein, we successfully synthesized 2D RP hybrid perovskites BMPB single crystals and investigated the relationship between the rectangular and hexagonal morphologies. Combining its excellent optoelectronic and ferroelectric properties, we designed a 5×5 optoelectronic memristor array. The device exhibited the responsivity of 0.96 A/W and detectivity of 2.89×10^8 Jones after polarization under 0 V bias and 410 nm illumination. In addition, as a memristor, the device showed an ultrahigh on/off ratio ($\sim10^5$), ultralow power consumption of ~ 82.8 pW, and a long retention time (>22 000 s). Finally, based on the optoelectronic memristor array and the construction of digital logic circuits, we successfully achieved the application of time prediction and monitoring of sunflower growth status, which is verified by Vivado simulation.

2 | Results and Discussion

Figure 1a illustrates the human visual system, in which light is received by photoreceptors in the retina and transmitted via the optic nerve to the visual cortex in the brain. Inspired by the human visual system, we designed a neuromorphic device based on BMPB perovskites. The memristive performance of 2D Ruddlesden–Popper perovskites $BA_2MAPb_2Br_7$ (BMPB, n = 2) is firstly reported. And the optoelectronic, memristive, and ferroelectric properties of BMPB are characterized in detail. By constructing the 5×5 array device, we successfully achieved the integrated functions of sensing, memory, and logic computing in the neuromorphic devices (Figure 1b). Figure 1c shows the optical image of 6 mm×5 mm BMPB rectangular single crystals which is synthesized using the quasi-static cooling method. The circuit diagram of the 5×5 array electrodes designed by L-edit is exhibited in Figure 1d. The 5×5 array device based on BMPB is illustrated in Figure 1e, which is fabricated via photolithography technology. Figure S1 illustrates the transfer process of BMPB perovskites, and the transferred perovskites can be used for further morphology and performance characterization. Figure 1f depicts the formation process and mechanism analysis of BMPB perovskites at the liquid–air interface. Due to the smaller surface nucleation energy at the liquid–air interface (Figure 1g), BMPB tends to preferentially nucleate and grow at the interface (Figure 1h). The in situ observation of the BMPB growth process is shown in Figure S2, revealing the growth of rectangular and hexagonal perovskite single crystals at the liquid–air interface. To verify the universality of the synthesis method, we further synthesized BA_2PbBr_4 (BPB, n = 1) and $MAPbBr_3$ (MPB, n = ∞) with different quantum well widths and successfully prepared corresponding perovskite single crystals (Figures S3 and S4). Interestingly, as the width of the quantum well approaches infinity (MPB), the morphology of perovskites transforms into a 3D type, which is consistent with previous reports [47].

Figure 2a shows the unit cell structure of BMPB, and from the unit cell model, it can be seen that the thickness of a single layer of BMPB is approximately 3.9 nm. Figure 2b displays the atomic force microscope (AFM) test image of BMPB. The BMPB single crystal exhibits a regular rectangular appearance and a flat surface, indicating good crystal quality. The edge step thickness of BMPB is approximately 19.3 nm, which is roughly the thickness of 5 layers. Figure 2c shows the X-ray diffraction (XRD) images of BA_2PbBr_4 (BPB) and BMPB. It can be seen that the nucleation direction of the hybrid perovskites with different quantum well widths n = 1 and n = 2 is along the (002) crystal plane. Figure 2d,e exhibit the different morphologies (rectangle and hexagon) of BMPB after crystallization. When the crystallization time is short (< 30 s), hexagonal single crystals tend to precipitate in the solution. When the crystallization time is long (> 30 s), the solution tends to precipitate rectangular single crystals.

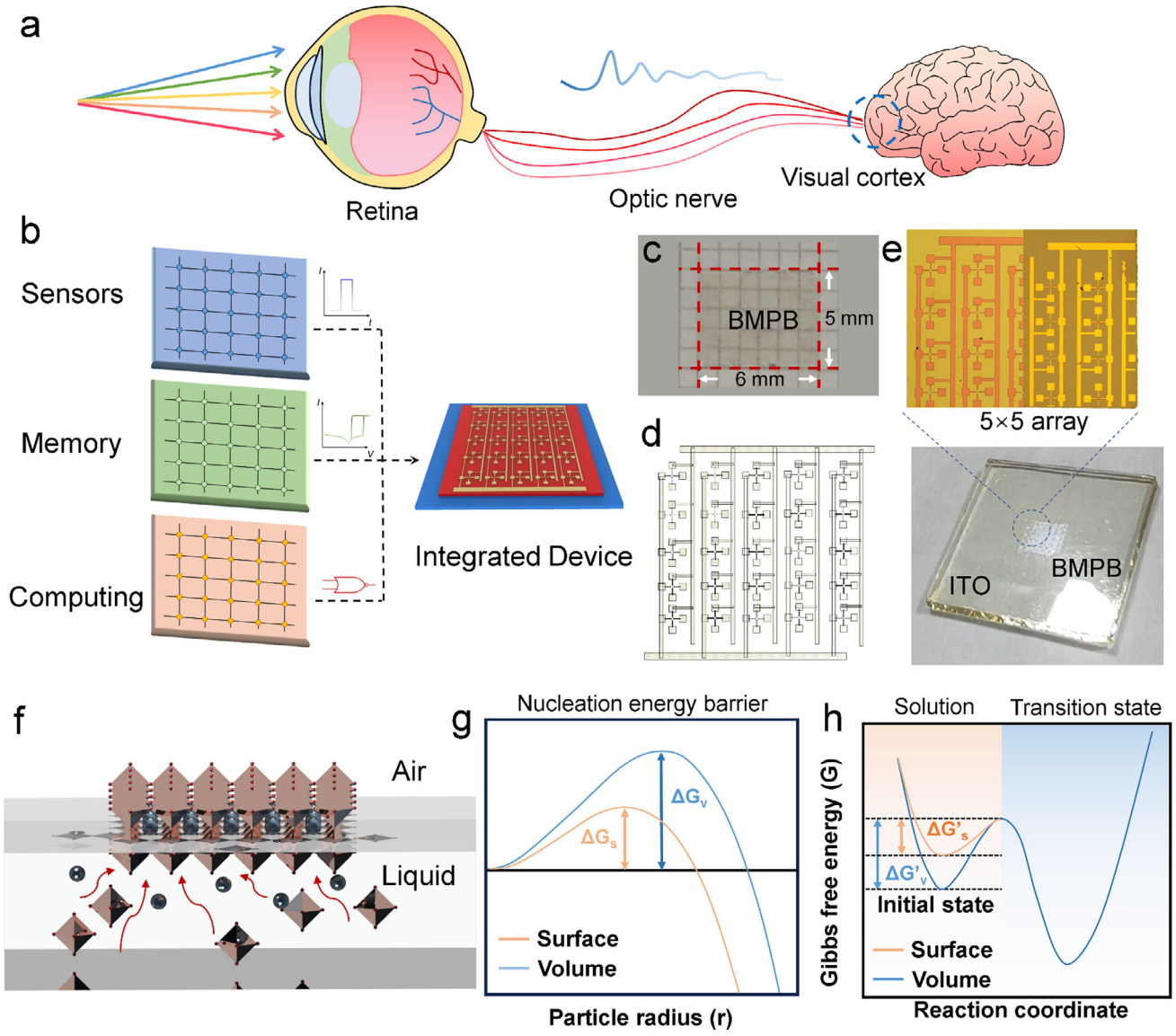

FIGURE 1 | Schematic diagram of an integrated array device based on BMPB perovskites and formation mechanism of BMPB perovskites. a) Schematic diagram of the biologic visual system. b) Schematic diagram of optoelectronic array sensor based on BMPB perovskites. BMPB combines sensing, storage, and computing functions, and can achieve logical computing functions. c) Optical image of BMPB perovskites with a size of 5 mm×6 mm. d) Array electrode circuit designed by L-edit. e) The optical image of the BMPB 5×5 array device. f) BMPB perovskites growing at the liquid air interface. g) Comparison of nucleation barriers between the solution surface and volume. h) Diagram illustrating the energy changes for the growth into crystal from precursor molecules.

Figure S5 shows a transition morphology from hexagonal to rectangular during the crystallization process. After the hexagonal single crystal transitions to an octagonal single crystal, it can further grow along the vertical direction of the edges, ultimately forming a rectangular single crystal. Figure S6 displays the optical and SEM images of BMPB perovskites after transferring process. Figure 2f exhibits the UV–vis absorption spectrum of BPB and BMPB perovskites. The absorption edge of BPB appears at approximately 425 nm, while the absorption edge of BMPB appears at approximately 440 and 450 nm. The appearance of multiple absorption edges in BMPB may be related to interlayer exciton effects [48]. The selected area electron diffraction (SAED) patterns (Figure 2g,h) display diffraction patterns of rectangular and hexagonal single crystals, where the (002) crystal plane is consistent with the results of XRD. Figure 2i illustrates the high-resolution transmission electron microscope (HRTEM) image of BMPB, with the inset image of the diffraction pattern after Fourier transform. The HRTEM image of BMPB shows clear lattice stripes. Its interplanar spacing is ~0.23 nm, which is in consistent of the interplanar spacing of the (002) crystal plane. Figure S7 exhibits the calculation process of the BMPB crystal plane spacing. Figure S8a shows the XPS survey spectra of BPB and BMPB perovskites, which is conducted to investigate the element composition and valence states. It can be seen that BPB and BMPB perovskites are composed of C, N, Pb, Br elements, and the appearance of O can be attributed to the oxidation effect of the surface. In the high-resolution spectra of C 1s (Figure S8b). The C—H bonds of BPB and BMPB are located at 283.81 and 284.22 eV,

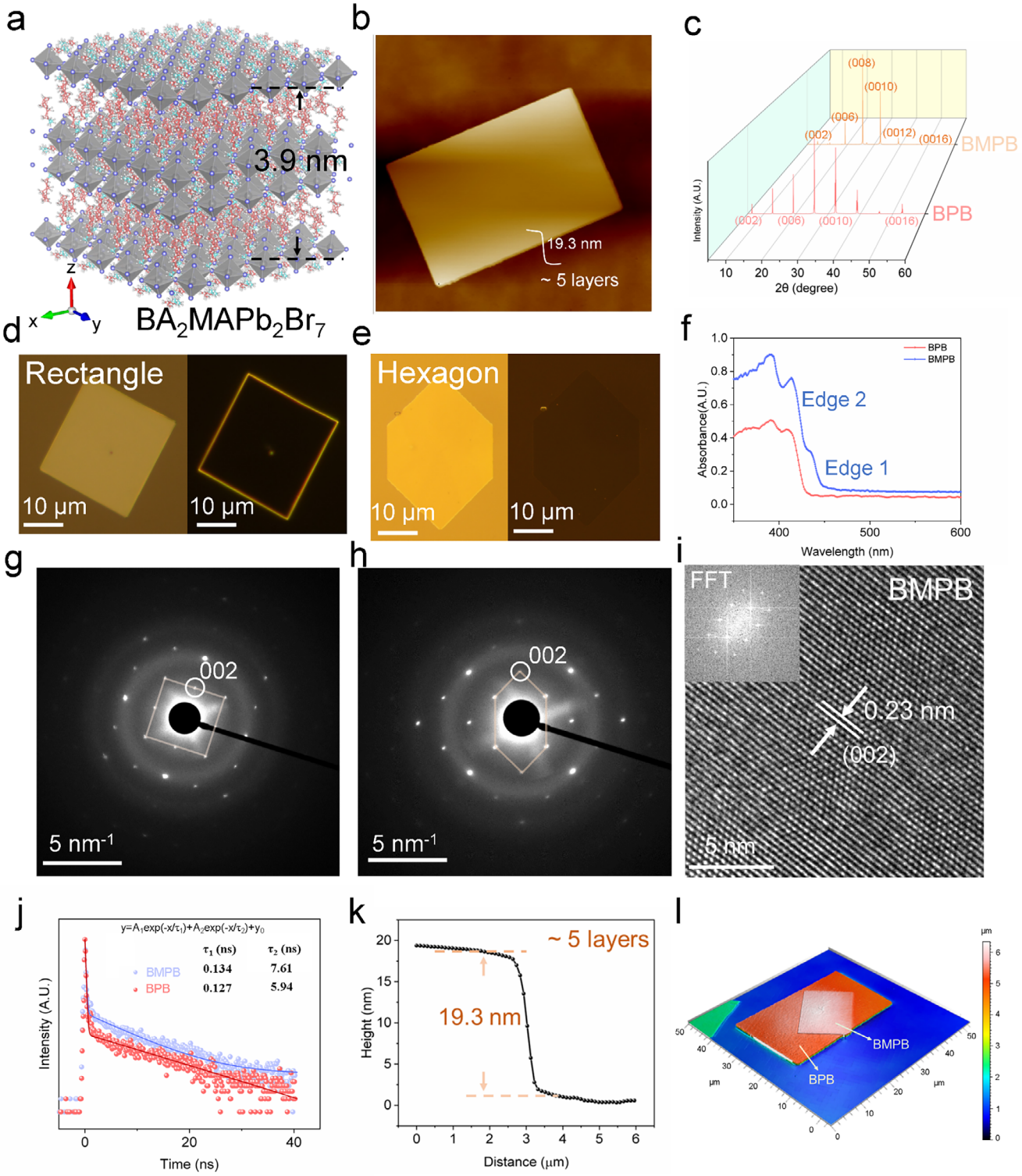

FIGURE 2 | Characterization of the morphology, structure, and carrier lifetime of BMPB perovskites. a) Molecular model diagram of BMPB perovskites. b) Atomic force microscope (AFM) image of BMPB. c) XRD patterns of BPB and BMPB perovskites. Optical image of BMPB single-crystals with d) rectangle and e) hexagon morphologies. f) UV–vis absorption spectrum of BPB and BMPB perovskites. SAED patterns of BMPB perovskites with g) rectangle shape and h) hexagon shape. scale bar: 5 nm^{-1}. i) High-resolution TEM image of BMPB single crystals. The inset shows the corresponding FFT image. j) Time-resolved photoluminescence (TRPL) spectra of BPB and BMPB perovskites excited by a 450 nm laser. k) Height curve of BMPB perovskites measured by atomic force microscope. l) The laser confocal 3D height imaging of BPB and BMPB perovskites.

respectively. Due to the presence of butyl groups in BMPB, it has a stronger electronegativity compared to the methyl group in BPB, resulting in a higher C—H bond binding energy. The C—C bonds of BPB and BMPB are located at 284.80 and 284.88 eV, respectively. As illustrated in Figure S8c, the N—H bonds of BPB and BMPB exhibit peaks at 400.85 and 401.30 eV, respectively. As shown in Figure S8d, the high-resolution spectra of Pb 4f in BPB and BMPB exhibit two pairs of peaks at 137.55, 142.45, and 138.08 and 142.96 eV, respectively. And they are corresponding to the characteristic doublet state Pb $4f_{7/2}$ and Pb $4f_{5/2}$. The ratio of peak area of the two satellite peaks is approximately 7:5. The high-resolution Br 3d XPS spectra of BPB and BMPB show two pairs of peaks at 67.55, 68.45 and 67.88, 68.83 eV (Figure S8e), corresponding to the characteristic doublet state Br $3d_{5/2}$ and Br $3d_{3/2}$. The ratio of the peak area in Br 3d satellite peaks is approximately 5:3. Valence band X-ray photoelectron spectroscopy (VB-XPS) tests are conducted to confirm the valence band (VB) position of BMPB. As illustrated in Figure S8f, the VB position is measured at 1.68 eV. Figure S9 supplements the Kelvin probe force microscopy (KPFM) characterization of the BMPB perovskites to further analyze the surface potential. It can be seen that compared to the Si substrate, BMPB has a lower surface potential of ∼200 mV. This indicates that the surface work function of BMPB is smaller than that of silicon, making it easier for electrons to escape. Figure S10 describes the elemental distribution of BMPB. It can be seen that BMPB is composed of elements C, N, Pb, and Br, and the elements are evenly distributed inside the perovskites. As depicted in Figure 2j, the time-resolved photoluminescence (TRPL) characterizations expound on the dynamics of photogenerated carriers in BPB and BMPB. The longer carrier life time ($\tau_1 = 0.134$ ns and $\tau_2 = 7.61$ ns) in the BMPB bi-exponential fitting curve indicates fewer recombination sites, which is conducive to efficient photodetection. Figure S11 presents the PL test results of BPB, BMPB, and their heterojunctions. It can be observed that the emission peak of BPB is approximately 412 nm, while the emission peak of BMPB is approximately located at 442 nm. After stacking to form a heterojunction, the peak positions are basically the same as the original positions. Figure S12 displays the schematic diagram of unit cells for BPB and BMPB perovskites. Figure 2k exhibits the edge height of BMPB single crystals measured by atomic force microscope, which is approximately 5 layers of BMPB unit cell. As depicted in Figure 2l, BPB and BMPB can be stacked to form a van der Waals heterojunction structure. The laser confocal image displays the size of the stack area and flat surface of BPB and BMPB. This structure is expected to be a platform for subsequent research on optics and carrier analysis in perovskites-type van der Waals heterojunctions. In addition, we further constructed BPB/BMPB heterojunctions with different stacking angles, providing ideas for subsequent research on superlattice systems based on 2D RP perovskites (Figure S13). The magnified AFM images of BPB and BMPB are shown in Figures S14 and S15, demonstrating that the surface flatness of the perovskite microplates obtained by the synthesis method in this experiment is excellent.

The architecture of the optoelectronic memristor device based on BMPB is displayed in Figure 3a, which was prepared by photolithography. This device can simultaneously function as a photodetector and a memristor, and the polarization process of BMPB can be achieved by applying a voltage to the anode. Figure S16 shows the photolithography process. The main process of photolithography technology includes spin-coating, UV exposure, development, deposition, and lift off. Due to the arbitrariness of photolithography pattern design, the potential for functional expansion in this experiment is high. Here, a 5×5 array device is designed for integrated sensing, memory, and computing. Figure S17 shows the photolithography pattern on a 6-inch silicon substrate, indicating the potential application of 2D RP perovskites in larger area array devices in the future. The molecular DFT calculations are employed to estimate dipole moments, utilizing the Gaussian code alongside the def2-TZVP basis set and the PBE functional. The calculated dipole moment of MA and BA molecules is 2.08 and 2.12 Debye, respectively (Figure 3b,c), and the values represent the charge distribution in the C, N, and H atoms, which contributes to the ferroelectric properties of BMPB. To investigate the memristor performance of the BMPB device, a typical I–V dual sweep is performed from −2.0 to 2.0 V as illustrated in Figure 3d. When the voltage increases to the set voltage (V_{set}∼1.2 V), the high resistance state (HRS) turns to the low resistance state (LRS) with a relatively low power consumption of P ∼ 82.8 pW ($P = V_{set} \times I_{set}$ = 1.2V×69 pA). Inversely, when the voltage decreases to the reset voltage (V_{reset}), the LRS switches back to HRS. The memristor reaches a large on/off ratio of $\sim 10^5$ under current compliance of 10 μA. While the device exhibits excellent retention and initial endurance, cycling beyond 50 cycles reveals a gradual decrease in the set and reset voltage. This is likely due to the cumulative effect of Ag^+ migration and vacancy redistribution, a known challenge in filamentary memristors. Future optimization, such as interface engineering or employing a pulsed operation mode, could significantly enhance the endurance. Nevertheless, for the target application of low-Hz, event-driven in-sensor computing, which requires infrequent weight updates, the current endurance is promising. In addition, to ascertain the stability and reliability of the BMPB memristor, the endurance test is conducted, and a long-term HRS and LRS retention of over 22 000 s is successfully realized under the condition of 0.05 V read voltage (Figure 3e). From the perspective that the resistance of the BMPB-memristor can still maintain the LRS state for a long time after power off, it is considered to be a non-volatile memristor. This is consistent with previous research findings based on 2D organic–inorganic hybrid perovskites [49]. To figure out the mechanism of the I-V switching mechanism, the ln (I) vs. ln (V) from the I-V curve is displayed in Figure 3f. When the device is in the LRS status, the linear fitting slope of ∼1 corresponds to the Ohmic law, indicating the appearance of highly conductive wires formed between the top Ag and bottom ITO electrode. When the device is in the HRS status, the fitting results of ln (I)∼$V^{1/2}$ suggest a conducting mechanism of Schottky contact. Figure 3g shows the set and reset voltages of the BMPB memristor during different cycling processes. It can be observed that the average value of set voltage is approximately 1.2 V, and the average value of reset voltage is approximately 0.2 V. In Figure 3h, BMPB perovskites present a typical P-E hysteresis loop (blue line) with saturated polarization (Ps) of 4.9 μC cm^{-2}. The current-electric field curve plotted next to the P—E hysteresis loop reveals two oppositely polarized peaks that originate from the switching of two different polarized states. The estimated coercive field (Ec) for the BMPB perovskites is ±23 kV cm^{-1}, corresponding to the P—E loop. Local PFM switching spectroscopy further demonstrates the robust ferroelectricity in BMPB perovskites, as exhibited in the 180°

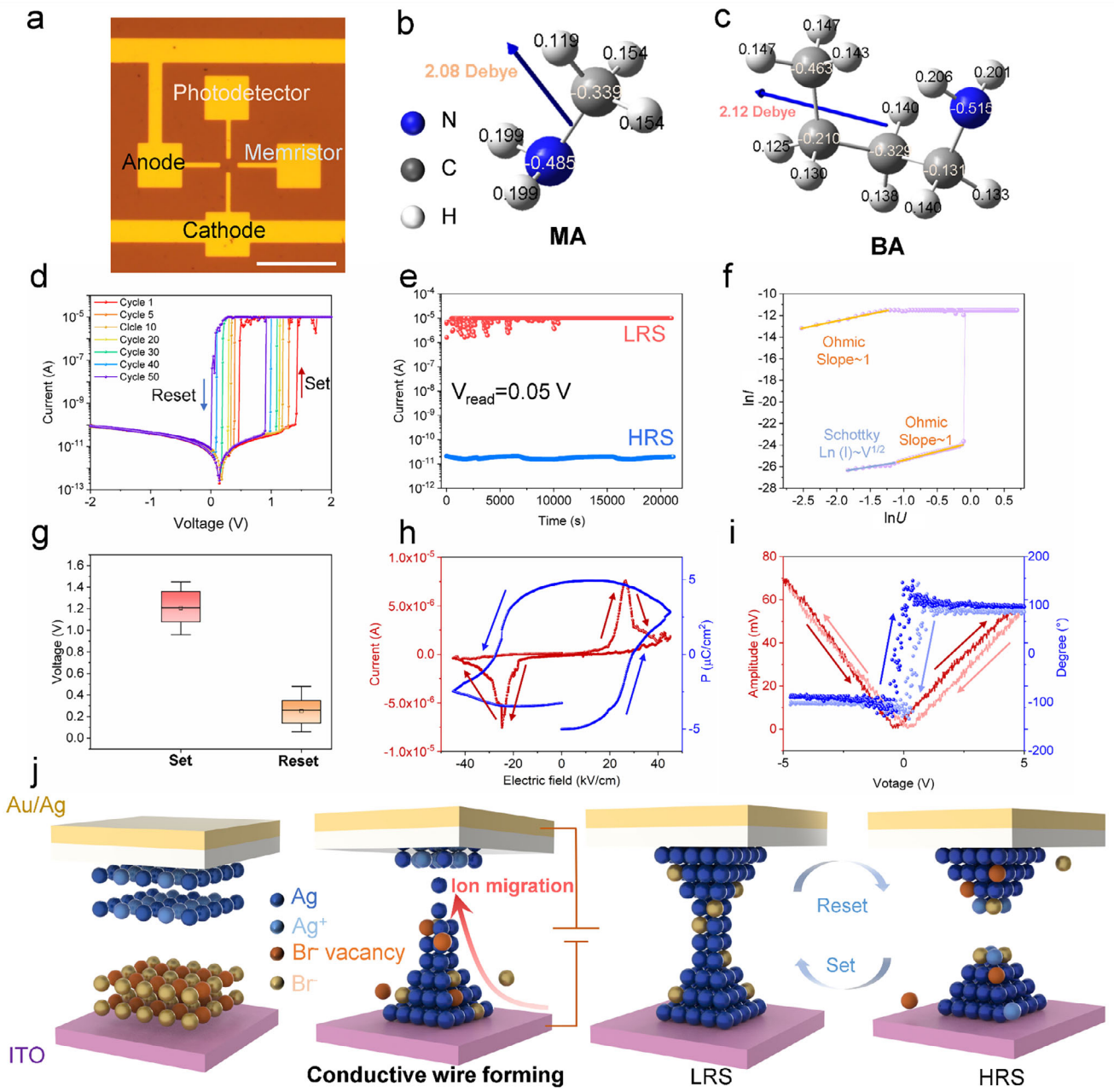

FIGURE 3 | Device structure and analysis of ferroelectric and memrisive performance. a) Optical microscopy image of an individual BMPB device. Scale bar: 100 μm. b,c) Optimized molecular structures and dipole moments of MA and BA via Gaussian quantum chemistry calculations. d) Resistive switching performance of the BMPB memristor of the 50-cycle sweeps. e) Characterization of retention time (LRS and HRS) at V_{read} of 0.05 V. f) ln (I) vs. ln (V) curve of BMPB perovskites. g) Statistics of the V_{set} and V_{reset} for the BMPB memristor. h) P–E hysteresis loop and I–E curve of BMPB perovskites. i) The butterfly-shaped piezoelectric force microscope (PFM) amplitude loop and 180°-reversed PFM phase loop of BMPB perovskites (the red and blue lines represent amplitude and phase change, respectively). j) Schematic of the resistive switching physical mechanism of BMPB memristor.

phase hysteresis and butterfly-shape amplitude loops (Figure 3i). The resistive switching mechanism is illustrated in Figure 3j. When the bias voltage increased, the Ag atoms in the top electrode can be oxidized into Ag^+ ions, which could further move to the bottom ITO electrode. After reaching the bottom ITO electrode, Ag^+ ions can be reduced to Ag atoms and simultaneously accumulate and grow toward the top electrode. At the same time, Br^- ions in the BMPB perovskites slowly migrate to the top Au/Ag electrode, creating abundant Br vacancies which contribute to the formation of a conductive filament. The device state turns to LRS. When the bias voltage decreased, Ag^+ ions in the conductive filament move back toward the top Au/Ag electrode, while Br^- ions migrate to the opposite bottom ITO electrode, leading to the rupture of the previous conductive filament. Finally, the device state turns back to HRS. The switching mechanism in the BMPB memristor may involve a synergistic interplay between ferroelectric polarization and electrochemical ion migration. The latter is responsible for the formation and rupture of the conductive filament, constituting the core resistive switching behavior. The former plays a critical modulatory role by lowering the energy barrier for ion migration, leading to reduced operating voltage and power consumption, enhancing the self-powered

photodetection capability via the ferroelectric-photovoltaic effect, and potentially localizing filament growth via domain structures, improving switching uniformity. Thus, the ferroelectric property is key to achieving the high-performance, energy-efficient, and multi-functional operation in our device.

Figure 4a shows the schematic and optical diagram of the BMPB array device. The basic structure of the device is that the top electrode is an array electrode of Au, the bottom electrode is ITO, and the functional layer is BMPB perovskites. Figure 4b displayed the *I-V* curves of BMPB based device and polarized-BMPB based device. It could be observed that the dark current at 0 V bias of BMPB based device and polarized-BMPB based device are 5.81×10^{-14} and 3.61×10^{-13} A. And the photocurrent at 0 V bias with 410 nm illumination are 7.48×10^{-11} and 8.56×10^{-10} A, respectively. Owing to the modulation on the conductive and valence bands of the self-polarized electric field, polarized-BMPB based device exhibits higher photocurrent after polarization. The high on/off ratio of 1.81×10^{4} in the polarized-BMPB based device is observed in the I-t curve (Figure 4c), which indicates that the BMPB responds effectively to incident 410 nm light. To further investigate the spectral performance of BMPB, the spectral responsivity (R_λ) and external quantum efficiency (EQE) are measured under varying wavelength and power densities of incident light.

R_λ describes the sensitivity of the photodetector to a specific wavelength optical signal, which is defined as the following formula [50]:

$$R\lambda = \frac{I_{ph} - I_{dark}}{P_\lambda S} \tag{1}$$

where I_{ph} is the photocurrent, I_{dark} is the dark current, P_λ is the light power density (1.7 μW/cm^2), and S is the effective irradiation area (5×10^{-4} cm^2). As shown in Figure 4d, self-powered BMPB PD exhibits highest R_λ of 0.96 A/W at 410 nm illumination.

$$R\lambda = \frac{8.56\times10-10\ A - 3.61\times10-13\ \mathrm{A}}{1.7\times10-6\ \mathrm{W/cm2}\times5\times10-4\ \mathrm{cm2}} = 0.96\ A/W \tag{2}$$

The relationship between photocurrent and incident power density is investigated, and it could be fitted by the power-law relationship [51]:

$$Ip = P\alpha \tag{3}$$

As exhibited in Figure 4e, when the incident light power density is within the linear region, the dependence index α of photocurrent on power density is approximately 0.997, indicating an excellent linear dependence relationship ($\alpha = 1$). While the incident light power density exceeds the linear region, the dependence index α of is 0.267, with the device entering the nonlinear dependence region.

Detectivity, denoted as D*, is a key figure-of-merit for photodetectors that quantifies their ability to detect weak optical signals [52]. It essentially describes the signal-to-noise performance of the detector, normalized by its active area and measurement bandwidth. The core concept is built upon the Noise-Equivalent Power (NEP), which is the incident optical power required to produce a signal equal to the detector's noise. In simpler terms, NEP is the minimum detectable power. Detectivity is defined as the reciprocal of NEP, normalized for area and bandwidth:

$$D* = \frac{\sqrt{S\times\Delta f}}{NEP} \tag{4}$$

where A is the detector's active area, Δf is the electrical bandwidth, and NEP is the noise-equivalent power.

In this work, the NEP is calculated as

$$NEP = \frac{\sqrt{i_n}}{R_\lambda} = 7.746\times10-11\ W/\sqrt{Hz} \tag{5))}$$

where noise current is 6×10^{-21} A^2/Hz as shown in Figure S19, and R_λ is 0.96 A/W.

From this value, the D* can be obtained as

$$D* = \frac{\sqrt{S\times\Delta f}}{NEP} = \frac{\sqrt{5\times10^{-4}\ cm^2\times1\ Hz}}{7.746\times10^{-11}\ W/\sqrt{Hz}} = 2.89\times108\ Jones \tag{6}$$

EQE is the ratio of photogenerated carriers to the number of incident photons, which could reflect the optoelectronic conversion efficiency of PDs. It can be calculated by the following formula [53]:

$$\mathrm{EQE} = \frac{hc}{e\lambda}R_\lambda \tag{7}$$

where h, c, and λ refer to the Planck constant, speed of light, and light wavelength.

As depicted in Figure 4f, BMPB PD displays the highest EQE of 280% at 410 nm illumination, indicating its excellent photon-electron conversion efficiency. The high EQE value may originate from the hole-trapping effect by surface oxygen adsorption, which enhances the carriers' lifetime and reduces the transit time between the electrodes [54]. The dominant photodetection mechanism may involve ferroelectric-field-driven charge separation and photoconductive gain, the latter arising from hole injection sustained by long-lived trapped electrons, which explains the EQE exceeding 100%. Figure 4g displays the statistical distribution of photocurrent across the array device and it can be seen that photocurrent distribution of the array device is relatively concentrated. Figure 4h shows the relationship of photocurrent and incident light wavelength. BMPB PD exhibits dual-band response characteristics at 370 and 410 nm, with bandwidths of 50 and 30 nm, respectively. The PD exhibits excellent photoelectric response from 300 to 550 nm, indicating its potential to operate under different wavelength optical signals. Figure S18 shows the current changes of BPB and $BA_2MA_2Pb_3Br_{10}$ ($n = 3$) at different wavelengths. It can be seen that the optimal response wavelength of BPB is approximately 390 and 430 nm, while the optimal response wavelength of $BA_2MA_2Pb_3Br_{10}$ ($n = 3$) is approximately 460 nm. Figure S19 illustrates noise current spectrum of BMPB perovskites during the frequency 1 to 10^5 Hz. Figure S20 displays the photocurrent variation curve of BMPB under different incident light power densities from 0.72 to 1204 μW/cm^2. Furthermore, as

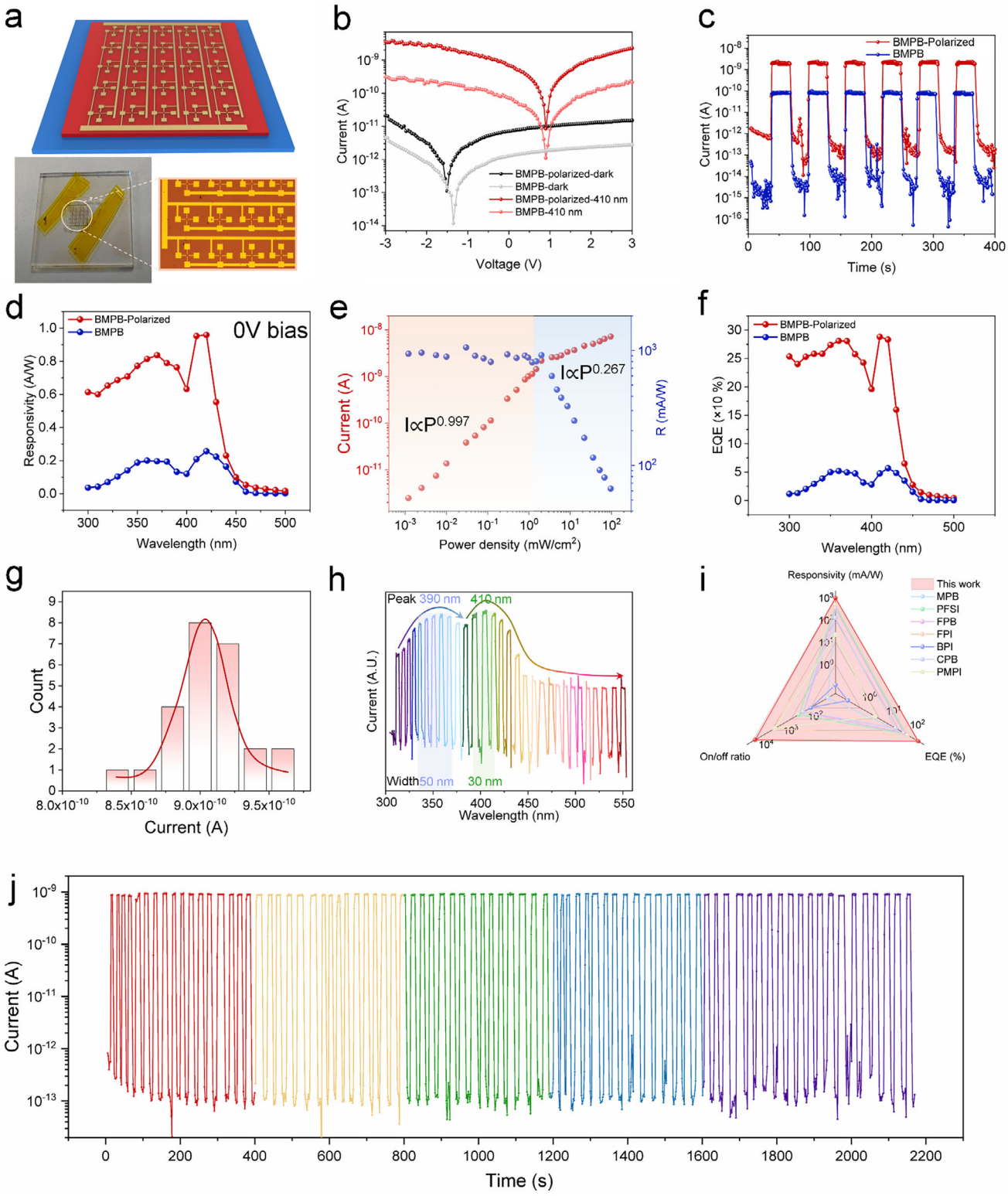

FIGURE 4 | Self-powered optoelectronic performance of BMPB perovskites. a) Schematic and optical diagrams of the array device. b) *I–V* curves in the dark and 410 nm illumination conditions. c) *I–t* curves at 0 V bias under 410 nm illumination of fresh and polarized states. d) The responsivity curve as a function of wavelength for BMPB perovskites. Bias: 0 V. e) Photocurrent and responsivity of BMPB perovskites at different laser power densities of 0 V bias at 410 nm illumination. f) EQE curve at 410 nm illumination of BMPB. Bias: 0 V. g) Statistical distribution of photocurrent across the 5×5 array. h) The photocurrent variation curves at different wavelengths from 300 to 550 nm. i) Responsivity, EQE, and on/off ratio comparison of BMPB PD and reported self-powered PDs in the previous studies. The reference data are from Table S1. j) Long term *I-t* curve of BMPB PD at 0 V bias.

demonstrated in Figure 4i and Table S1, the BMPB PD in our work shows superior responsivity and on/off ratio compared with other self-powered PDs based on 2D perovskites. To evaluate the stability and reliability of BMPB PD, long term I-t test is conducted and it can be seen that the photocurrent after 2100 s (9.13×10^{-10} A) is still 98.3% of the initial value (9.29×10^{-10} A), which demonstrates the excellent stability of BMPB PD. Table S2 further compares the performance comparison between recently reported perovskites-based memristors and BMPB-based memristors in our work. Figure S21 displays the comparison of power consumption and retention time of memristive devices reported in recent literature (shown in Table S2) with this work. It can be seen that BMPB in this work shows competitive power consumption (~ 82.8 pW) and long stability. When benchmarked against the state-of-the-art, the BMPB device demonstrates a unique position. While its endurance is currently lower than mature oxide memristors [55], its ultralow power consumption is competitive [56]. More critically, its responsivity rivals specialized photodetectors [57], yet this high-performance sensing is integrated monolithically with non-volatile memory. This synergy, absent in most reported devices, enables the demonstrated in-sensor computing paradigm without the energy cost of data movement. This work establishes 2D RP perovskites as a promising material platform for highly integrated neuromorphic vision systems. The ultralow power consumption of the individual BMPB memristor is the cornerstone for energy-efficient system operation. When integrated into an in-sensor computing array, the system-level power advantage is twofold. First, the aggregate power of the active device array itself remains in the nanowatt range. Second, and more significantly, this architecture obviates the need for energetically costly data movement between separate sensors, memory, and processors, which can dominate total system energy in conventional von Neumann systems. Thus, the pW-level device performance directly enables a system-level paradigm with orders-of-magnitude lower energy consumption for edge vision tasks.

In order to verify the integrated sensing, storage, and computing capabilities of the device, an application scenario is designed based on sunflower monitoring. Figure 5a depicts sunflowers with different orientations and growth states at different times. By detecting and imaging the posture feature information of sunflowers, the BMPB photoelectric array device can achieve the function of predicting time and detecting the growth status of sunflowers (Figure 5b). Figure S22 illustrates the process of using array electrodes to construct AND, OR, and NOT logic circuits. Through the series connection, parallel connection, and bias voltage regulation between array electrodes, we successfully achieved AND, OR, and NOT logic operations, and further integrated XOR gates and XNOR gates based on AND, OR, and NOT logic gates. The AND, OR, and NOT logic circuit electrodes prepared by the photolithography process are shown in Figure S23. The I-t curves measured in the AND, OR, and NOT logic circuits are shown in Figure 5c–e. In Figure 5c, when there is no incident light irradiation or only one electrode is irradiated with incident light, the output photocurrent is less than 10^{-11}A, and the output signal is defined as 0. When two electrodes are simultaneously irradiated with incident light, the output photocurrent is greater than 10^{-11}A, and the output signal is defined as 1. As shown in Figure 5d, when there is no incident light irradiation, the output photocurrent is less than 10^{-11}A, and the output signal is defined as 0. When any electrode is irradiated with incident light, the output photocurrent is greater than 10^{-11}A, and the output signal is defined as 1. As displayed in Figure 5e, when there is no incident light irradiation, the output photocurrent is greater than 0 nA, and the output signal is defined as 1. When there is incident light irradiation, the output photocurrent is less than −0.8 nA, and the output signal is defined as 0. In order to transmit the information of photocurrent images to smart electronic devices, we design a digital logic circuit as exhibited in Figure 5f. The photocurrent information is input as high or low level voltage in logic circuits, and after conversion through AND gates, OR gates, XOR gates and AND gates, we successfully achieved the output of time prediction and growth status. Figure S24 displays the truth table of AND, OR, NOT, NOR and XNOR gates. Figure 5g illustrates the detection scenario of sunflowers using BMPB optoelectronic array devices. First, using a 5×5 array device, the stem part of the sunflower is imaged. Then, the photocurrent is input as a high and low voltage signal to the digital logic circuit, and finally, time prediction and growth status information are output. The signals for time prediction are displayed in red, orange, and green, corresponding to morning, noon, and evening. The signals of growth status are displayed as light blue, deep blue, and purple, corresponding to juvenile, developmental, and mature stages, respectively. The inset table shows the correspondence between a set of input signals and output signals. To verify the above design concept, we conducted a simulation using Vivado. Figure S25 is the code used in the simulation process, and Figure S26 is the input–output waveform obtained from the simulation, which demonstrates that the above designed circuit can achieve dual functions of time prediction and growth monitoring. Finally, we successfully implemented the application of photoelectric detection devices in time prediction and growth state detection, providing useful ideas for the design of integrated devices based on BMPB for the function of sensing, storage, and computing in the future. While the 5×5 array successfully demonstrates the integrated sensing-memory-computing concept, scaling to larger arrays for real-world imaging presents challenges in uniformity, crosstalk, and fabrication yield. Based on our results, the intrinsic material uniformity of BMPB is promising. Future work will focus on developing wafer-scale in situ crystallization techniques to replace manual transfer, integrating a 1T1R cell structure to eliminate crosstalk, and employing design-for-manufacturing principles to achieve high yield. The low-temperature processing and strong performance of our BMPB devices provide a solid foundation for these scaling efforts. In addition, we supplemented in situ observation of BMPB single crystals for one month. The obtained optical microscope variation images are shown in Figures S27 and S28. When the BMPB single crystal was transferred on a PDMS substrate, BMPB maintained a highly stable morphology during a month long observation. However, after transferring BMPB to the gold electrode, significant decomposition occurred after 7 days, which may be due to the accelerated decomposition process of BMPB upon contact between the metal and BMPB. Correspondingly, as shown in Figure S29, in the optoelectronic performance testing of BMPB devices, the I-t curve remained relatively stable in the first 7 days. But after 7 days, there was a significant decline in optoelectronic performance. All tests were conducted at room temperature and in an air environment. To clarify the discrepancy between the volatile-like switching in dynamic I-V sweeps and the

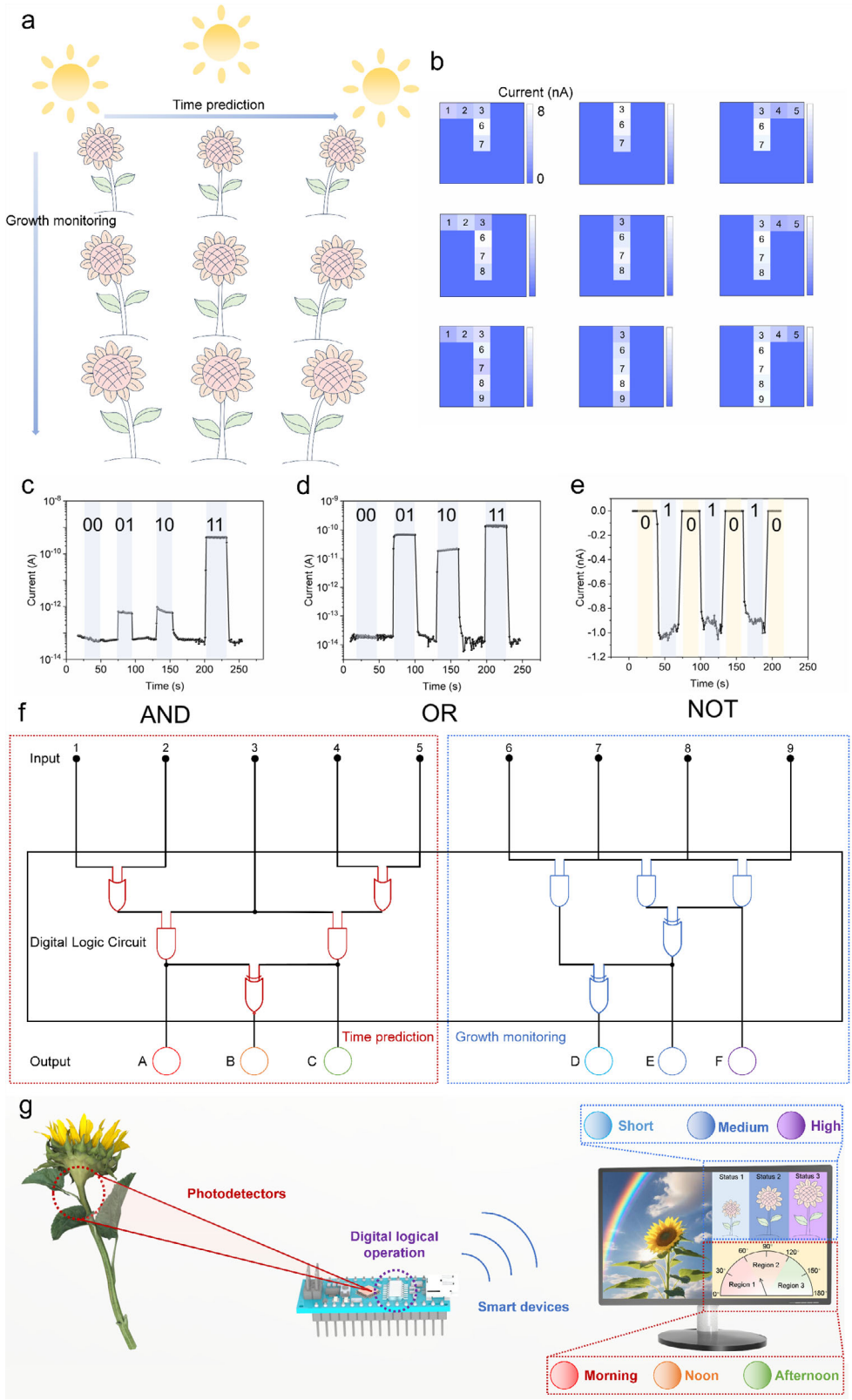

FIGURE 5 | Application diagram of time prediction and growth status monitoring in a sunflower scene. a) Schematic diagram of the application scene. b) The 5×5 image pattern obtained from the array device. c) Current-time curve in AND logic circuits. d) Current-time curve in OR logic circuits. e) Current-time curve in NOT logic circuits. f) Design a schematic of a digital logic circuit. g) Accurate imaging and signal transmission process of sunflowers using array devices.

non-volatile retention, we conducted a systematic investigation into the evolution of the resistive switching behavior. The initial cycles exhibit the Ohmic conduction (Figure S30a), which transitions to an asymmetric curve indicative of a Schottky barrier in subsequent cycles (Figure S30b), before stabilizing into a consistent, non-volatile unipolar memristive switching characteristic (Figure S30c). Crucially, extended retention measurements over 18 h at 0.05 V read voltage demonstrate excellent stability for both the LRS (Figure S30d) and HRS (Figure S30e), confirming their non-volatile nature. The complete SET-RESET cycle observed within a single voltage sweep arises from the metastability of the freshly formed Ag filament. One possible explanation of the resistive switching mechanism is that during the downward sweep of the bias, the combined drive from the decreasing external field, the internal ferroelectric field, and concentration gradients can rupture the nascent filament. In contrast, under a constant and low read voltage, the reverse driving force is minimized, allowing the filament to remain stable.

3 | Conclusion

In conclusion, 2D RP perovskite BMPB is successfully synthesized, and the memristive and optoelectronic performance is thoroughly characterized. As a memristor, the BMPB perovskites achieved an ultrahigh on/off ratio (~10^5), ultralow power consumption of ~82.8 pW, and a long retention time (>22 000 s). As a photodetector, it exhibited responsivity of 0.96 A/W, detectivity of 2.89×10^8 Jones, on/off ratio of 1.81×10^4, and robust stability (98.3% photocurrent retention rate after 2100 s) at 0 V bias and 410 nm illumination. By constructing a low power consumption 5×5 optoelectronic memristor array and digital logic circuits, we successfully realized the function of time prediction andgrowth status monitoring of sunflower, which is verified by Vivado simulation. This application provides new insights for the future application of 2D RP hybrid perovskites in smart devices such as smartphones, computers, and bracelets.

4 | Experimental Section

4.1 | Reagents

BABr (99.99%), MABr (99.99%), $PbBr_2$ (≥98.0%), Hydrobromic acid (HBr, 55.0-58.0% in H_2O, contains≤1.5%H_3PO_2), PT (70:30, mol%) were used as reagents without further treatment.

Crystal growth and device construction

4.2 | Crystal Growth

Single-crystalline BMPB was synthesized from concentrated HBr solutions containing stoichiometric quantities of BABr (1.131 g), MABr (0.414 g), and $PbBr_2$ (2.697 g). The clear solutions were obtained after reaction for 15 min at 120°C. Large-size single crystals were grown by the temperature lowering method from a saturated solution. The cooling rate was 1°C/day. The high-quality crystals could be obtained after 60 days.

4.3 | Device Construction

After preparing large perovskite single crystals (5 mm×6 mm), transfer the perovskites onto ITO glass, fix the crystal with polyimide tape, and then polarize the ferroelectric perovskites using electrospinning equipment (E = 40 kV/cm). Then 5×5 array gold electrodes on top of perovskites are prepared using photolithography technology for subsequent testing.

4.4 | Materials Characterization and Ferroelectric-Optoelectronic Measurement

The optical images were captured by an Olympus microscope. PL spectra were acquired by Renishaw inVia-Qontor Raman microscope equipped with 325 and 532 nm lasers. Transmission electron microscope (TEM, JEM-F200), high-resolution TEM (HRTEM), and selected area electron diffraction (SAED) were used to characterize the crystal structure. The composition determination of crystal materials was carried out by a Bruker D8 Advance X-ray Power diffractometer (XRD, Cu-Kα radiation source, λ = 0.15406 nm). The optical properties were obtained using a UV–vis spectrometer (Hitachi U-3900H) and an FLS1000 fluorescence spectrometer. XPS spectra were obtained using Thermo ESCALAB 250XI under the excitation of Al Kα (energy = 1486.6 eV, voltage = 15 kV, beam current = 10 mA). The height and roughness data were measured by a step profiler (Bruker DektakXT) and an atomic-force microscope (AFM). A KPFM AtomExplorer from Truth Instruments Company (Qingdao) was used for topographic characterization. The morphologies of perovskite microplates were obtained by using a ZEISS laser scanning confocal microscope (LSM 900). A dual channel precision sourcemeter (2902A, Keysight) was used for the electrical measurement in air. The domain patterns obtained after poling using positive/negative voltages were inspected via out-plane piezoresponse force microscopy (PFM) amplitude and phase imaging (Icon, Bruker) using a contact PtIr-coated silicon tip with a radius of ~20 nm, a force constant of 2.8 N/m, and an AC amplitude of 1 V at 386 kHz. The optoelectronic properties were collected using the semiconductor characterization system (Keithley 4200-SCS) connected to a vacuum probe station (Lake Shore), and a 75 W Xe lamp equipped with a monochromator was used as a light source. The light density was measured by a NOVA II power meter (OPHIR photonics). The wavelength and light intensity used in the PDs comparison are 410 nm and 1.7 μW/cm^2, and the effective illumination area is 5×10^{-4} cm^2. The testing of noise current spectrum based on the semiconductor parameter analyzer FS-Pro with the testing range of 1-10^5 Hz. All the optoelectronic and memristive measurements, including the I-V, I-t, and spectral response characteristics, were performed at room temperature and under ambient atmospheric conditions unless otherwise specified.

Acknowledgements

The work was supported by the National Key R&D Program of China (No. 2022YFA1402904), National Natural Science Foundation of China (No. 52425308, 62374035 and 92263106). The authors thank Dr. Zijun Hu, Xueshuo Fan, Feng Yuan and Dr. Jie Liu for their kind help in this manuscript.

Conflicts of Interest

The authors declare no conflicts of interest.

Data Availability Statement

The data that support the findings of this study are available in the Supplementary Material of this article.

References

1. F. Cao, Z. Hu, T. Yan, et al., "A Dual-Functional Perovskite-Based Photodetector and Memristor for Visual Memory," *Advanced Materials* 35 (2023): 2304550, https://doi.org/10.1002/adma.202304550.

2. B. Ouyang, J. Wang, G. Zeng, et al., "Bioinspired in-Sensor Spectral Adaptation for Perceiving Spectrally Distinctive Features," *Nature Electronics* 7 (2024): 705–713, https://doi.org/10.1038/s41928-024-01208-x.

3. Z. Wang, T. Wan, S. Ma, and Y. Chai, "Multidimensional Vision Sensors for Information Processing," *Nature Nanotechnology* 19 (2024): 919–930, https://doi.org/10.1038/s41565-024-01665-7.

4. C. Fuentes-Hernandez, W.-F. Chou, T. M. Khan, et al., "Large-Area Low-Noise Flexible Organic Photodiodes for Detecting Faint Visible Light," *Science* 370 (2020): 698–701, https://doi.org/10.1126/science.aba2624.

5. H. Ning, Z. Yu, Q. Zhang, et al., "An in-memory Computing Architecture Based on a Duplex Two-Dimensional Material Structure for in Situ Machine Learning," *Nature Nanotechnology* 18 (2023): 493–500, https://doi.org/10.1038/s41565-023-01343-0.

6. X. Xu, Y. Chen, P. Liu, et al., "General Synthesis of Ionic-Electronic Coupled Two-Dimensional Materials," *Nature Communications* 15 (2024): 4368, https://doi.org/10.1038/s41467-024-48690-7.

7. Z. Zhao, Z. Hu, M. Deng, et al., "Bias-Switchable Photodetection and Photosynapse Dual-Functional Devices Based on 2D Perovskite/Organic Heterojunction for Imaging-to-Recognition Conversion," *Advanced Materials* 37 (2025): 2416033, https://doi.org/10.1002/adma.202416033.

8. M. Deng, Z. Li, S. Liu, X. S. Fang, and L. Wu, "Wafer-scale Integration of Two-Dimensional Perovskite Oxides towards Motion Recognition," *Nature Communications* 15 (2024): 8789, https://doi.org/10.1038/s41467-024-52840-2.

9. H. Huang, X. Liang, Y. Wang, et al., "Fully Integrated Multi-Mode Optoelectronic Memristor Array for Diversified in-Sensor Computing," *Nature Nanotechnology* 20 (2025): 93–103, https://doi.org/10.1038/s41565-024-01794-z.

10. G. Wu, X. Zhang, G. Feng, et al., "Ferroelectric-Defined Reconfigurable Homojunctions for in-Memory Sensing and Computing," *Nature Materials* 22 (2023): 1499–1506, https://doi.org/10.1038/s41563-023-01676-0.

11. F. Cao, Y. Liu, X. Zhang, et al., "Lead-Free Single Crystal Metal Halide Perovskite Detectors," *Materials Science and Engineering: R: Reports* 164 (2025): 100991, https://doi.org/10.1016/j.mser.2025.100991.

12. X. Zhang, Y. Long, N. Lu, et al., "Moiré Superlattice in Two-Dimensional Materials: Fundamentals, Applications, and Recent Developments," *ACS Applied Materials & Interfaces* 16 (2024): 68724–68748, https://doi.org/10.1021/acsami.4c13135.

13. J. Liu, W. Han, E. Hong, et al., "In-Memory Sensing and Logic Processing in Negative Capacitance Phototransistors," *Advanced Functional Materials* 35 (2025): 2425350, https://doi.org/10.1002/adfm.202425350.

14. S. Wu, J. Deng, X. Wang, et al., "Polarization Photodetectors with Configurable Polarity Transition Enabled by Programmable Ferroelectric-Doping Patterns," *Nature Communications* 15 (2024): 8743, https://doi.org/10.1038/s41467-024-52877-3.

15. S. Chen, S. Wang, Z. Liu, et al., "Channel and Contact Length Scaling of Two-dimensional Transistors Using Composite Metal Electrodes," *Nature Electronics* 8 (2025): 394–402, https://doi.org/10.1038/s41928-025-01382-6.

16. Y. Zhang, Y. Chen, G. Liu, et al., "Nonalloyed α-Phase Formamidinium Lead Triiodide Solar Cells through Iodine Intercalation," *Science* 387 (2025): 284–290, https://doi.org/10.1126/science.ads8968.

17. H. Yin, M. Liao, Y. Shi, et al., "Close-to-Equilibrium Crystallization for Large-Scale and High-Quality Perovskite Single Crystals," *Advanced Materials* 37 (2025): 2415957, https://doi.org/10.1002/adma.202415957.

18. W. Cheng, S. Wu, J. Lu, et al., "Self-Powered Wide-Narrow Bandgap-Laminated Perovskite Photodetector with Bipolar Photoresponse for Secure Optical Communication," *Advanced Materials* 36 (2024): 2307534, https://doi.org/10.1002/adma.202307534.

19. T. Sun, R. Chen, W. Ma, et al., "Van der Waals Quaternary Oxides for Tunable Low-loss Anisotropic Polaritonics," *Nature Nanotechnology* 19 (2024): 758–765, https://doi.org/10.1038/s41565-024-01628-y.

20. S. Han, J. Bie, W. Fa, et al., "Field-Induced Antiferroelectric–Ferroelectric Transformation in Organometallic Perovskite Displaying Giant Negative Electrocaloric Effect," *Journal of the American Chemical Society* 146 (2024): 8298–8307, https://doi.org/10.1021/jacs.3c13422.

21. F. Sui, H. Li, R. Qi, et al., "Atomic-Level Polarization Reversal in Sliding Ferroelectric Semiconductors," *Nature Communications* 15 (2024): 3799, https://doi.org/10.1038/s41467-024-48218-z.

22. D. Pan, Y. Fu, N. Spitha, et al., "Deterministic Fabrication of Arbitrary Vertical Heterostructures of Two-Dimensional Ruddlesden–Popper Halide Perovskites," *Nature Nanotechnology* 16 (2021): 159–165, https://doi.org/10.1038/s41565-020-00802-2.

23. X. Zeng, Y. Liu, W. Weng, et al., "A Molecular Pyroelectric Enabling Broadband Photo-pyroelectric Effect towards Self-driven Wide Spectral Photodetection," *Nature Communications* 14 (2023): 5821, https://doi.org/10.1038/s41467-023-41523-z.

24. H. Xu, F. Sun, W. Guo, et al., "Building Block-Inspired Hybrid Perovskite Derivatives for Ferroelectric Channel Layers with Gate-Tunable Memory Behavior," *Angewandte Chemie International Edition* 62 (2023): 202309416, https://doi.org/10.1002/anie.202309416.

25. X. Zhao, Z. Li, S. Wang, et al., "2-Bromonaphthalene-Induced Defect Passivation to Suppress Ion Migration in $CsPbBr_3$ Wafer for X-Ray Detector with Bias-Resistant Stability," *Advanced Functional Materials* 35 (2025): 2500039, https://doi.org/10.1002/adfm.202500039.

26. Z. Xu, X. Dong, L. Wang, et al., "Precisely Tailoring a $FAPbI_3$-Derived Ferroelectric for Sensitive Self-Driven Broad-Spectrum Polarized Photodetection," *Journal of the American Chemical Society* 145 (2023): 1524–1529, https://doi.org/10.1021/jacs.2c12300.

27. X. Zhang, E. Hong, X. Tan, J. Liu, A. Jiang, and X. S. Fang, "2D Ruddlesden-Popper Perovskites/PVDF-TrFE Photodetector for Anti-Interference Vision System Derived From Ferroelectric Polarization Modulation," *Advanced Functional Materials* 35 (2025): 2424848, https://doi.org/10.1002/adfm.202424848.

28. X. Zhang, Z. Li, E. Hong, M. Deng, L. Su, and X. S. Fang, "Modulating Quantum Well Width of Ferroelectric Ruddlesden–Popper Perovskites for Flexible Light Communication Device," *Advanced Functional Materials* 34 (2023): 2312293, https://doi.org/10.1002/adfm.202312293.

29. R. Xing, X. Zhang, X. Fan, R. Xie, L. Wu, and X. S. Fang, "Coupling Strategies of Multi-Physical Fields in 2D Materials-Based Photodetectors," *Advanced Materials* 37 (2025): 2501833, https://doi.org/10.1002/adma.202501833.

30. T. Yan, Z. Li, F. Cao, J. Chen, L. Wu, and X. S. Fang, "An All-Organic Self-Powered Photodetector with Ultraflexible Dual-Polarity Output for Biosignal Detection," *Advanced Materials* 34 (2022): 2201303, https://doi.org/10.1002/adma.202201303.

31. B. Dang, T. Zhang, X. Wu, K. Liu, R. Huang, and Y. Yang, "Reconfigurable in-Sensor Processing Based on a Multi-Phototransistor–One-Memristor Array," *Nature Electronics* 7 (2024): 991–1003, https://doi.org/10.1038/s41928-024-01280-3.

32. X. Yan, Z. Zheng, V. K. Sangwan, et al., "Moiré Synaptic Transistor with Room-Temperature Neuromorphic Functionality," *Nature* 624 (2023): 551–556, https://doi.org/10.1038/s41586-023-06791-1.

33. S. S. Teja Nibhanupudi, A. Roy, D. Veksler, et al., "Ultra-Fast Switching Memristors Based on Two-Dimensional Materials," *Nature Communications* 15 (2024): 2334, https://doi.org/10.1038/s41467-024-46372-y.

34. R.-Y. Sun, Z.-Y. Hou, Q. Chen, et al., "Orientation-Selective Memory Switching in Quasi-1D $NbSe_3$ Neuromorphic Device for Omnibearing Motion Detection," *Advanced Materials* 37 (2025): 2409017, https://doi.org/10.1002/adma.202409017.

35. Z. Wang, S. Joshi, S. E. Savel'ev, et al., "Memristors with Diffusive Dynamics as Synaptic Emulators for Neuromorphic Computing," *Nature Materials* 16 (2017): 101–108, https://doi.org/10.1038/nmat4756.

36. W. Wang, Y. Wang, F. Yin, et al., "Tailoring Classical Conditioning Behavior in TiO_2 Nanowires: ZnO QDs-Based Optoelectronic Memristors for Neuromorphic Hardware," *Nano-Micro Letters* 16 (2024): 133, https://doi.org/10.1007/s40820-024-01338-z.

37. Y. Cheng, J. Zhang, Y. Lin, et al., "Bioinspired Adaptive Neuron Enabled by Self-Powered Optoelectronic Memristor and Threshold Switching Memory for Neuromorphic Visual System," *Advanced Science* 12 (2025): 2417461, https://doi.org/10.1002/advs.202417461.

38. Q. Zhang, Q. Che, F. Xuan, and B. Zhang, "Donor-Redox Covalent Organic Framework-Based Memristors for Visual Neuromorphic System," *InfoMat* 7 (2025): 70035, https://doi.org/10.1002/inf2.70035.

39. Y. Huang, W. Yang, P.-K. Zhou, et al., "Intermolecular Hydrogen-Bond Stabilized 1D Pyrene-Based Covalent Organic Framework for Advanced Memory Devices and Neuromorphic Computing," *Advanced Functional Materials* 35 (2025): 2505890, https://doi.org/10.1002/adfm.202505890.

40. J. Li, B. Zhang, B. Zhou, et al., "Covalent Organic Framework-based Photoelectric Dual-modulated Memristors for Wafer Surface Quality Evaluation," *Matter* 8 (2025): 102197, https://doi.org/10.1016/j.matt.2025.102197.

41. B. Jiang, X. Chen, X. Pan, et al., "Advances in Metal Halide Perovskite Memristors: A Review from a Co-Design Perspective," *Advanced Science* 12 (2025): 2409291, https://doi.org/10.1002/advs.202409291.

42. S. Panchanan, S. Dutta, G. Dastgeer, R. Jaafreh, K. Hamad, and S. I. Seok, "Mixed-Dimensional Cu-Based Perovskites for Stable and Energy-Efficient Neuromorphic Memristors," *Advanced Functional Materials* 35 (2025): 2520665, https://doi.org/10.1002/adfm.202520665.

43. Y. Wang, S. Chen, X. Cheng, et al., "Neurotransmitter-Mediated Plasticity in 2D Perovskite Memristor for Reinforcement Learning," *Advanced Functional Materials* 34 (2023): 2309807, https://doi.org/10.1002/adfm.202309807.

44. Z. Hu, Y. Hu, L. Su, and X. S. Fang, "Light-adaptive Mimicking Retina With In Situ Image Memorization via Resistive Switching Photomemristor Arrays," *Laser & Photonics Reviews* 18 (2024): 2301364, https://doi.org/10.1002/lpor.202301364.

45. D. Cui, P. Guo, Y. Xu, et al., "Self-Powered Halide Perovskite Optoelectronic Synaptic Memristors for Reconfigurable Logic and Reservoir Computing Applications," *Nano Letters* 25 (2025): 15705–15713, https://doi.org/10.1021/acs.nanolett.5c04297.

46. J. Pan, J. Hu, X. Dong, et al., "Enhancement of Stability and Durability in Nanocrystal Memristors With Surface Defect Control for Image Encryption and Storage," *Advanced Functional Materials* 35 (2025): 2500765, https://doi.org/10.1002/adfm.202500765.

47. X. Fan, E. Hong, P. Wang, and X. S. Fang, "Controlled Growth of 2D-3D Perovskite Lateral Heterostructures for Wavelength-Tunable Light Communication," *Advanced Functional Materials* 35 (2024): 2415491, https://doi.org/10.1002/adfm.202415491.

48. E. Hong, Z. Li, X. Zhang, and X. S. Fang, "Light-State Rectification Behaviors Induced by Interlayer Excitons in Mixed-Dimensional Single-Crystalline Perovskite Heterostructures," *Advanced Functional Materials* 35 (2024): 2412189, https://doi.org/10.1002/adfm.202412189.

49. K. S. Keremane, A. Gorthy, L. Zheng, et al., "Molecularly Engineered Highly Stable Memristors with Ultra-Low Operational Voltage: Integrating Synthetic DNA with Quasi-2D Perovskites," *Advanced Functional Materials* 36 (2026): 30539, https://doi.org/10.1002/adfm.202530539.

50. S. Li, X. Liu, H. Yang, H. Zhu, and X. S. Fang, "Two-dimensional Perovskite Oxide as a Photoactive High-κ Gate Dielectric," *Nature Electronics* 7 (2024): 216–224, https://doi.org/10.1038/s41928-024-01129-9.

51. X. Liu, S. Li, Z. Li, et al., "Boosted Responsivity and Tunable Spectral Response in B-Site Substituted 2D $Ca_2Nb_{3-x}Ta_xO_{10}$ Perovskite Photodetectors," *Advanced Functional Materials* 31 (2021): 2101480, https://doi.org/10.1002/adfm.202101480.

52. V. Pecunia, T. D. Anthopoulos, A. Armin, et al., "Guidelines for Accurate Evaluation of Photodetectors Based on Emerging Semiconductor Technologies," *Nature Photonics* 19 (2025): 1178–1188, https://doi.org/10.1038/s41566-025-01759-1.

53. J. Wolansky, C. Hoffmann, M. Panhans, et al., "Sensitive Self-Driven Single-Component Organic Photodetector Based on Vapor-Deposited Small Molecules," *Advanced Materials* 36 (2024): 2402834, https://doi.org/10.1002/adma.202402834.

54. S. Li, Y. Zhang, W. Yang, H. Liu, and X. S. Fang, "2D Perovskite $Sr_2Nb_3O_{10}$ for High-Performance UV Photodetectors," *Advanced Materials* 32 (2020): 1905443, https://doi.org/10.1002/adma.201905443.

55. S. O. Park, H. Jeong, S. Seo, Y. Kwon, J. Lee, and S. Choi, "Experimental Demonstration of Third-order Memristor-based Artificial Sensory Nervous System for Neuro-inspired Robotics," *Nature Communications* 16 (2025): 5754, https://doi.org/10.1038/s41467-025-60818-x.

56. Y. H. Jang, J. Han, J. Kim, et al., "Graph Analysis with Multifunctional Self-Rectifying Memristive Crossbar Array," *Advanced Materials* 35 (2023): 2209503, https://doi.org/10.1002/adma.202209503.

57. R. Xing, Z. Li, W. Zhao, et al., "Waterproof and Flexible Perovskite Photodetector Enabled By P-type Organic Molecular Rubrene with High Moisture and Mechanical Stability," *Advanced Materials* 36 (2024): 2310248, https://doi.org/10.1002/adma.202310248.

Supporting Information

Additional supporting information can be found online in the Supporting Information section.

Supporting File: adma72621-sup-0001-SuppMat.pdf.